DIRECT NUMERICAL SIMULATION OF FLOW ACROSS A COMPLIANT BLUFF BODY

Takahide Endo, Ryutaro Himeno
Computer & Information Division. Institute of Physical & Chemical Research (RIKEN)
Hirosawa 2-1, Wako-shi, Saitama, 351-0198, Japan
tendo@postman.riken.go.jp, himeno@postman.riken.go.jp

ABSTRACT

A direct numerical simulation (DNS) code is constructed for solving flow across a three-dimensional deformable bluff body. In the present study, DNS of flow across rigid and compliant cylinders is performed to evaluate the code and the drag reduction effect with a compliant surface. The Strouhal number of shedding of the Karman vortex is calculated and it agrees well with that reported in the literature. Several cases changing the material properties of modelled compliant surface are calculated. It is shown that although the pressure drag is increased, the friction drag is reduced with compliant surface. This fact indicates that a compliant surface can be applied as a drag reduction device in friction drag dominant flows, such as flow around a huge ship.

INTRODUCTION

From the viewpoint of saving power and protecting the environment, it is highly desirable to develop efficient turbulence control techniques for drag reduction and heat transfer augmentation. Among various methodologies, active feedback control of turbulence attracts much attention because of its large control effect (Moin and Bewley, 1994; Gad-el-Hak, 1996; Kasagi, 1998). However, active control requires power input and maintenance, which may lead to drawbacks in real application.

Organisms living in water, on the other hand, have developed efficient turbulence control techniques through their unique evolutionary backgrounds. A typical example is the shark. The scales of a shark have grooves in the streamwise direction; a riblet surface is designed based on the shark's scales as a drag reduction device. The flow control techniques of undersea creatures are categorized as those of passive control (Bushnell and Hefner 1990; Gad-el-Hak, 1996), in which no control input is required. Therefore, it is easier to use passive control in real applications than active control.

A dolphin swims as fast as 40 knots per hour at the maximum. However, its muscles are not sufficiently strong to achieve such fast swimming (Gray, 1936); this is known as "Gray's paradox". Therefore, it is expected that the flexible skin of a dolphin (a compliant surface) plays a key role in controlling the surrounding fluid flow. Research studies of compliant surfaces were initiated by Kramer (1960), and it has been reported that a compliant surface causes transition delay and friction drag reduction.

Many experiments and numerical calculations using the Orr-Sommerfeld equation have been conducted to investigate the transition delay on compliant surfaces (e.g., Gad-el-Hak, 1996; Bushnell *et al.*, 1977; Riley *et al.*, 1988). Carpenter and Garrad (1985) modeled a compliant surface to an elastic plate which is supported by an array of springs, and found that the transitional Reynolds number increased.

On the other hand, a friction drag reduction of more than 20% was reported by Kramer (1960) and Chu and Blick (1969). However, the reliability of these results is open to question with respect to the accuracy of the measurement. No detailed data have been obtained, because there are many difficulties faced in conducting experiments over compliant surfaces; *i.e.*, the material properties are sensitive to changes in the environment of the experimental facility, and it is difficult to measure the flow field over a moving boundary.

Recently, Endo and Himeno (2001, 2002) developed the DNS code of turbulent channel flow over a compliant surface in order to investigate the friction drag reduction effect. They showed that a friction drag reduction of as much as 7% at maximum, and 3% on average is possible when the material properties are set such that the wall velocity is in phase with wall pressure fluctuation.

It is necessary to investigate the effect on the flow across a bluff body covered by a compliant surface, in order to apply the compliant surface to a flow control device on a real vessel and vehicles. The influence of a compliant surface on pressure drag has not yet been clarified, to the best of our knowledge. Here, flow across a cylinder is suitable to investigate the pressure drag, since there are enormous accumulation of numerical and experimental data for the flow across a rigid cylinder. We have developed a DNS code to simulate flow across a compliant cylinder.

The objective of the present study is to obtain detailed data on the flow field across a deformable compliant bluff body with the aid of DNS. The final goal is to propose an optimal combination of the material properties of the compliant coating on the bluff body to decrease the drag force on the body.

NUMERICAL CALCULATIONS

The governing equations are the incompressive Navier-Stokes equations and the continuity equation. The deformation of the cylinder is described with a boundary-fitted coordinate system for a moving boundary. The first-order implicit Euler scheme is used to integrate the Navier-Stokes

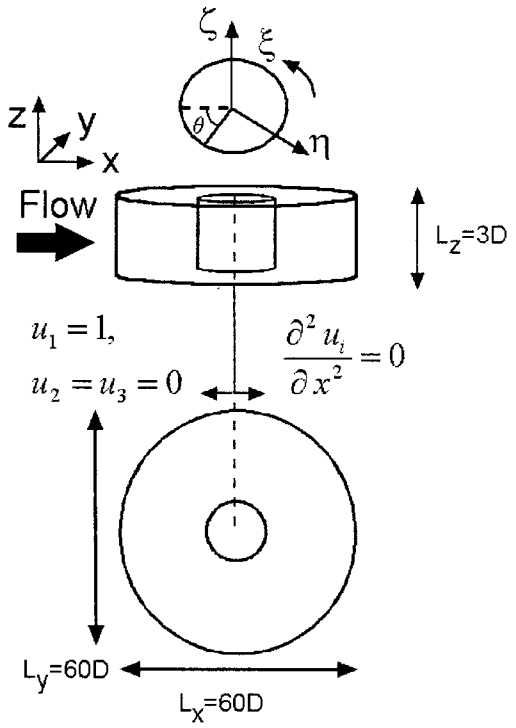

Figure 1: Schematic of calculation domain and coordinate system.

equation.

$$\frac{\boldsymbol{v}^{n+1} - \boldsymbol{v}^n}{\triangle t} + \left(\boldsymbol{v}^{n+1} \cdot \nabla\right) \boldsymbol{v}^{n+1} = -\nabla p + \frac{1}{Re} \triangle \boldsymbol{v}^{n+1}. \quad (1)$$

The second term of the left hand side of Eq. (1) is linearlized for $\boldsymbol{v}^{n+1}$ as follows;

$$\frac{\boldsymbol{v}^{n+1} - \boldsymbol{v}^n}{\triangle t} + \left(\boldsymbol{v}^{n} \cdot \nabla\right) \boldsymbol{v}^{n+1} = -\nabla p + \frac{1}{Re} \triangle \boldsymbol{v}^{n+1}. \quad (2)$$

All spatial derivatives except nonlinear terms in Eq. (2) are discretized by 2nd-order central difference method. On the other hand, nonlinear terms are approximated by the 3rd-order upwind scheme.

The 3rd-order upwind scheme in the curvilinear coordinate system is discretized as follows (Kawamura and Kuwahara, 1984);

$$\left(U \frac{\partial u}{\partial \xi}\right)_{i,j,k} = U_{i,j,k} \frac{-u_{i+2,j,k} + 8\left(u_{i+1,j,k} - u_{i-1,j,k}\right) + u_{i-2,j,k}}{12\triangle \xi} + \left|U_{i,j,k}\right| \frac{u_{i+2,j,k} - 4u_{i+1,j,k} + 6u_{i,j,k} - 4u_{i-1,j,k} + u_{i-2,j,k}}{4\triangle \xi}, \quad (3)$$

where U denotes the contravariant velocity, and defined as $U = (\partial \eta^1)/(\partial x_j) v_j$.

The nonslip boundary condition is adopted on the cylinder surface. Homogeneous laminar flow is imposed on the upstream side of the outer boundary with the velocity of U_∞, and the 2nd-derivative of the both pressure and velocity field in the streamwise direction is set to be zero on the downstream side of the outer boundary, as schematically shown in Figure 1. The pressure Poisson equation is solved with the multigrid method (Demuren and Ibraheem, 1998), where the Jacobi method is adopted for the finer and coarser meshes.

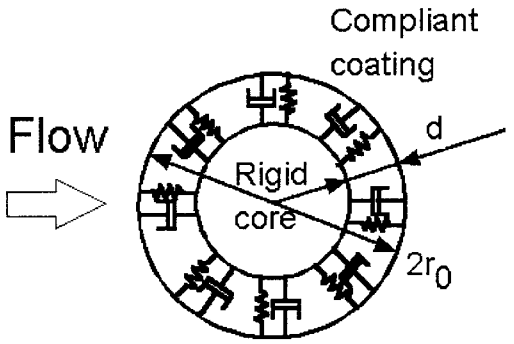

Figure 2: Schematic model for a compliant surface.

The computational domain is given as a cylinder, as schematically shown in Fig. 1. The measurements for computational volume are $60D$ both in the streamwise $(x-)$ and perpendicular to the flow $(y-)$ directions, and $3D$ in the spanwise $(z-)$ direction, where $D = 2r_0$ is the diameter of the cylinder. We chose an ordinal O-type grid system in the $x-y$ plane, and uniform meshes in the $z-$ direction. A cylindrical coordinate system was also used for ease of comprehension, where $\xi-$ denotes circumferential, $\eta-$ radial, and $\zeta-$ spanwise direction, respectively. Note that $\zeta-$ is the same as the $z-$ direction. The numbers of grid points used in the present study are relatively small to reduce the computational load, and are $N_\xi = 160, N_\eta = 101$ and $N_\zeta = 11$ in the $\xi-, \eta-$ and $\zeta-$directions, respectively.

Hereafter, all the parameters are non-dimensionalized by the inlet velocity U_∞ and the diameter of the cylinder D. The computational time step is $\triangle t = 0.01$. The Reynolds number based on U_∞ and D is $Re \equiv U_\infty D/\nu = 80$. A fully developed instantaneous flow field was used as the initial condition.

MODELING OF COMPLIANT SURFACE

In the first stage of the present study, the material property of the compliant surface is assumed to be isotropic. Carpenter and Morris (1990) found that the anisotropy of deformation of a compliant surface on a boundary layer contributes to the stabilization of the traveling-wave flutter (TWF) in boundary layer. However, a simple model of a compliant surface is used in the present study to investigate the influence of deformation of a compliant surface on the flow separation. Each grid point on the surface of the compliant cylinder is assumed to move only in the radial $(\eta-)$ direction, and the deformation of the compliant coating covering the rigid core is modeled by a spring, mass, and damper system (Fig. 2). The wall displacement is deter-

Table 1: Parameters and change of drag coefficients.

	ζ	ω_0	$\triangle C_{px}$	$\triangle C_{\tau x}$	$\triangle C_D$
Case 1	0.08	1	+82.86	+14.65	+63.53
Case 2-a	0.00	5	+17.48	-2.59	+11.79
Case 2-b	0.01		+16.52	-2.56	+11.11
Case 2-c	0.04		+14.19	-2.40	+9.48
Case 2-d	0.08		+11.95	-2.15	+7.95
Case 2-e	0.16		+9.10	-1.74	+6.03
Case 2-f	0.24		+7.37	-1.46	+4.87
Case 2-g	1.00		+2.63	-0.58	+1.72
Case 2-h	3.00		+0.97	-0.23	+0.63
Case 2-i	5.00		+0.60	-0.14	+0.39
Case 2-j	7.00		+0.43	-0.10	+0.28
Case 3-a	0.08	10	+3.07	-0.67	+2.01
Case 3-b	0.16		+2.84	-0.62	+1.86
Case 3-c	0.24		+2.65	-0.58	+1.73

mined as follows:

$$m\frac{\partial^2 r}{\partial t^2} + c\frac{\partial r}{\partial t} + k\,(r - r_0) = (P_\eta - \tilde{P}_\eta) + \Delta\xi\Delta\zeta\left(T_\xi\frac{\partial^2 r}{\partial \xi^2} + T_\zeta\frac{\partial^2 r}{\partial \zeta^2}\right), \quad (4)$$

where m is the mass of a compliant surface for one calculation grid volume, and is determined as $m \equiv \rho_c \cdot \Delta\zeta \cdot \pi\{D^2 - (D-d)^2\}/N_\xi$ (ρ_c is the density of a compliant surface). The parameters c and k are the damping parameter and the spring stiffness. And T_ξ and T_ζ are tensions employed in the $\xi-$ and $\zeta-$directions, respectively.

In Eq. (1), the drive force of the compliant surface is the wall pressure and friction drag in the radial component, and is defined as

$$P_\eta \equiv \frac{-\left\{\alpha^{12}\tau_{12} + \alpha^{22}\tau_{22} + \alpha^{23}\tau_{23}\right\}}{\sqrt{(\alpha^{12})^2 + (\alpha^{22})^2 + (\alpha^{23})^2}}, \quad (5)$$

where $\tau_{ij} = -p\delta_{ij} + (1/Re)\,(u_{i,j} + u_{j,i})$ is a stress tensor; $\alpha^{ij} \equiv (1/J)(\partial\eta^i)/(\partial x_m)\cdot(\partial\eta^j)/(\partial x_m)$ is a metric tensor, and J is the Jacobian of the grid. In order to keep the volume of the cylinder constant, the circumferential averaged value of driving force ($\tilde{P}_\eta$) is subtracted in the first term on the RHS of Eq. (4).

Equation (4) is non-dimensionalized by U_∞ and D as follows;

$$\frac{\partial^2 r^*}{\partial t^{*2}} + 2\zeta^*\frac{\partial r^*}{\partial t^*} + \omega_0^{*2}\left(r^* - \frac{1}{2}\right) = (P_\eta^* - \tilde{P}_\eta^*) + \frac{1}{\rho^* d^*}\left(T_\xi^*\frac{\partial^2 r^*}{\partial \xi^{*2}} + T_\zeta^*\frac{\partial^2 r^*}{\partial \zeta^{*2}}\right), \quad (6)$$

where the superscript $*$ denotes the non-dimensionalized value, however, it is omitted hereafter for simplicity.

It is evident that many parameters need to be determined in Eq. (6). The material properties of the compliant surface used in the present study are $d = 0.5r_0$, and density of the compliant surface ρ_c is same as that of the surrounding fluid; *i.e.*, $\rho^* \equiv \rho_c/\rho_f = 1.0$, and these are set to be constant. The tensions T_ξ and T_ζ are neglected for simplicity. The remaining parameters ζ and ω_0 are under investigation.

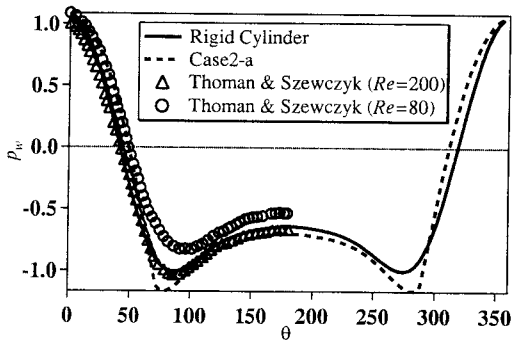

Figure 3: Mean pressure distribution.

RESULTS AND DISCUSSION

As the first stage of the present study, we tested quite a low Reynolds number flow of $Re = 80$, so that the influence of compliant surface on both pressure and friction drag is easily observed. In this case, it is well known that the Karman vortex is shed alternatively from the cylinder and that the flow pattern is two dimensional.

The Strouhal number is calculated for the flow across a rigid cylinder in order to evaluate the DNS code. The Strouhal number is defined as $S_t \equiv f \cdot D/U_\infty$, where f is the frequency of emission of the Karman vortex. The Strouhal number presently calculated is $S_t = 0.159$ for rigid cylinder. Liu *et al.*(1995) reported that the Strouhal number of the flow across a rigid cylinder at $Re = 105$, is $S_t = 0.156$. Tritton (1959) and Kovasznay (1949) reported that the number is close to 0.16 based on the results of their experiments. Therefore, the Strouhal number obtained in this simulation agrees well with these numerical and experimental results.

Table 1 shows several combinations of non-dimensionalized damping coefficient ζ and spring stiffness ω_0 in Eq. (6), which we have tested with the present DNS.

Figure 3 shows the wall pressure distribution on the rigid cylinder and compliant cylinder surfaces. The numerical results reported by Thoman and Szewczyk (1969) of $Re = 40$ and 200 are also plotted in the figure. The wall pressure distribution on the rigid cylinder in the present calculation is found to be between those of the lower and higher Reynolds number flow calculated by Thoman and Szewczyk, therefore the present calculation is confirmed to be reasonable. The negative peak values of the wall pressure on the compliant cylinder are lower than those on the rigid cylinder. As it is shown later, the compliant cylinder becomes flat near the stagnation point ($\theta = 0$), therefore, the wall pressure on the compliant cylinder near the stagnation point takes higher value than that on the rigid cylinder, and the wall pressure shows lower value on the downstream side.

Figure 4 shows the mean radial component of wall stress as defined in Eq. (5) on the rigid and compliant cylinders. Positive P_η indicates that the force is toward the outer direction of the cylinder. The mean radial component of wall stress P_η on the compliant cylinder shows higher peaks at $\theta \sim 75°$ and 285° than that on the rigid cylinder. This indicates that the cylinder surface affects tensions in radial direction at $\theta = 75°$ and 285°.

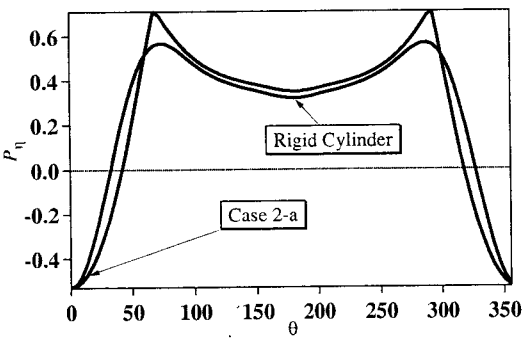

Figure 4: Distribution of mean radial component of stress.

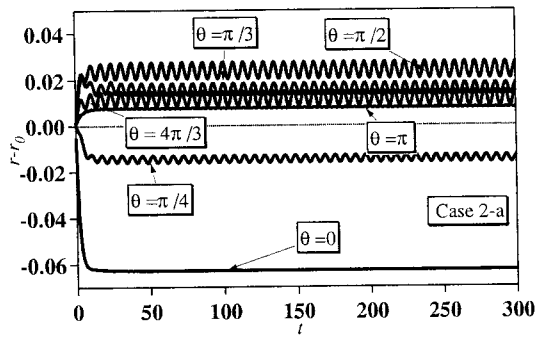

Figure 5: Time traces of wall deformation in case 2-a.

Figure 5 shows the time trace of wall deformation $r - r_0$ at $\theta = 0, \pi/4, \pi/3, \pi/2, 4\pi/3, \pi/2$ and π in Case 2-a. The displacement is almost constant at $\theta = 0, \pi$ except for the initial stage. At other points, the displacement shows quite small fluctuation.

Figure 6 shows the mean displacement distribution in Cases 2-a, 2-b, and 2-c. The displacement becomes smaller as damping parameter ζ becomes larger. Although it is not shown here, the displacement is smaller as the spring stiffness becomes larger.

Figure 7 shows the instantaneous wall displacement and velocity field on the $x-y$ plane at $z = 0$ near the compliant cylinder at $t^* = 300$ in Case 2-d. Although it is not shown here, the flow pattern is confirmed to be completely two dimensional. The wall color shows the instantaneous wall displacement of the cylinder, and the top of the cylinder (i.e., $\theta = 0$) forms a flat shape against to the flow as shown in Fig. 6. And the Karman vortex sheets is emitted alternatively.

Each component of the drag coefficient $C_D \equiv P_\eta / \frac{1}{2}\rho_f U_\infty^2$ (where ρ_f is density of the fluid) is divided into two parts, as follows,

$$C_D = C_{Dp} + C_{D\tau}, \tag{7}$$

where C_{Dp} denotes the coefficient of pressure drag, and $C_{D\tau}$ that of friction drag. The $x-$, $y-$ and $z-$ components of C_D

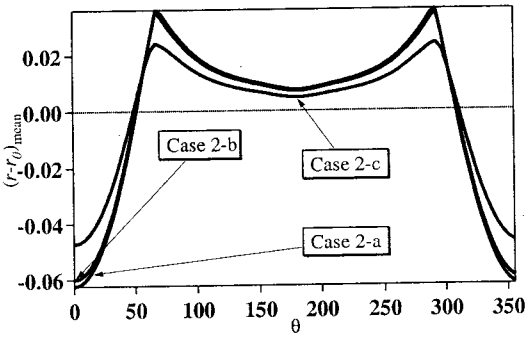

Figure 6: Distributions of mean deformation.

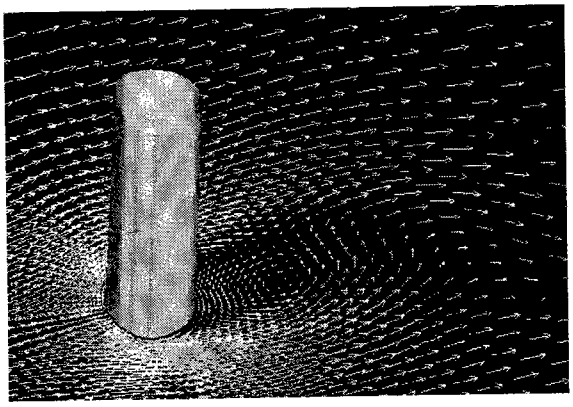

Figure 7: Instantaneous flow field and deformation of the compliant cylinder in case 2-d.

are calculated as follows,

$$\begin{bmatrix} C_{Dx} \\ C_{Dy} \\ C_{Dz} \end{bmatrix} = \begin{bmatrix} -p & 0 & 0 \\ 0 & -p & 0 \\ 0 & 0 & -p \end{bmatrix} \begin{bmatrix} \mathbf{e_x^n} \\ \mathbf{e_y^n} \\ \mathbf{e_z^n} \end{bmatrix} + \begin{bmatrix} \frac{2}{Re}\frac{\partial u}{\partial x} & \frac{1}{Re}\left(\frac{\partial u}{\partial y}+\frac{\partial v}{\partial x}\right) & \frac{1}{Re}\left(\frac{\partial u}{\partial z}+\frac{\partial w}{\partial x}\right) \\ \frac{1}{Re}\left(\frac{\partial u}{\partial y}+\frac{\partial v}{\partial x}\right) & \frac{2}{Re}\frac{\partial v}{\partial y} & \frac{1}{Re}\left(\frac{\partial v}{\partial z}+\frac{\partial w}{\partial y}\right) \\ \frac{1}{Re}\left(\frac{\partial u}{\partial z}+\frac{\partial w}{\partial x}\right) & \frac{1}{Re}\left(\frac{\partial v}{\partial z}+\frac{\partial w}{\partial y}\right) & \frac{2}{Re}\frac{\partial w}{\partial z} \end{bmatrix} \cdot \begin{bmatrix} \mathbf{e_x^n} \\ \mathbf{e_y^n} \\ \mathbf{e_z^n} \end{bmatrix}, \tag{8}$$

where $(\mathbf{e_x^n}, \mathbf{e_y^n}, \mathbf{e_z^n})$ is the normal unit vector on the cylinder surface.

Figure 8 (a) shows the $x-$ component of the coefficient of pressure drag C_{p_x} for the rigid and compliant cylinders. For compliant cylinder, three cases where the damping parameter is same, are compared. In case 1, although it is not shown here, the deformation is quite large, and the pressure drag increases up to twice of that in the rigid cylinder. In Cases 2-d, and 3-a, pressure drag increases as much as 12% and 3%, respectively. The cylinder becomes flat shape near the stagnation point (*i.e.*; $\theta = 0$), and it is expected this flat shape results in the increase of pressure drag.

Figure 8 (b) shows the $x-$ component of the coefficient of pressure drag C_{p_x} for the rigid and compliant cylinders,

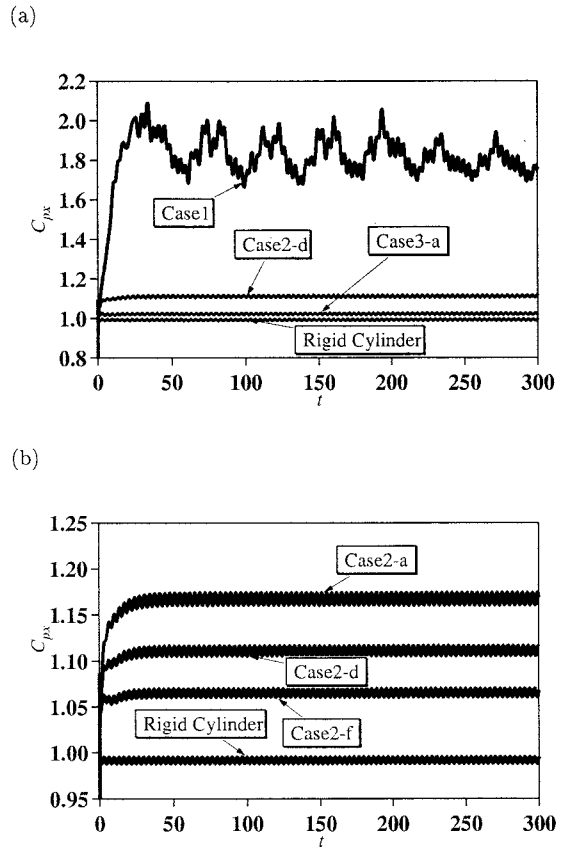

Figure 8: Time trace of the $x-$ component of the pressure drag coefficient. (a) The damping parameter ζ is constant, (b) The spring stiffness ω_0 is constant.

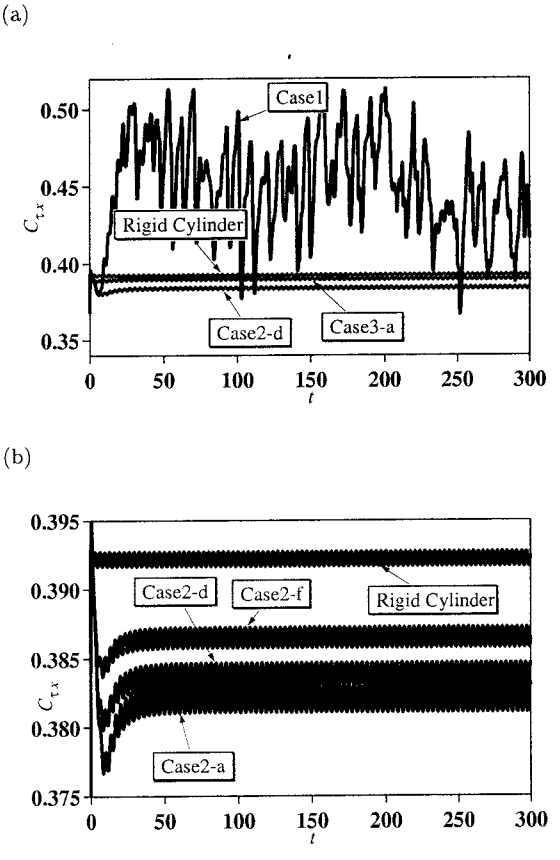

Figure 9: Time trace of the $x-$ component of the friction drag coefficient. (a) The damping parameter ζ is constant, (b) The spring stiffness ω_0 is constant.

where the spring stiffness ω_0 is same. We have tested several cases changing the damping parameter ζ in the same spring stiffness $\omega_0 = 5$ as tabled in Table 1 (Case 2-a to 2-j). As the damping parameter is smaller, the increase of pressure drag becomes larger. It is because the deformation of the compliant surface becomes large when the damping parameter is small, and hence, the shape of cylinder becomes flat near the stagnation point.

Figure 9 (a) shows the time trace of the friction drag coefficient $C_{\tau x}$ for rigid and three compliant cylinders where the damping parameter ζ is same. The friction drag is increased about 15% on average in Case 1. On the other hand, in Cases 2-d and 3-a, the friction drag is reduced. The friction drag reduction rate is much higher in Case 2-d than in Case 3-a. When the spring stiffness is larger than $\omega_0 = 10$, the change of friction drag is almost negligible. Therefore, it is expected that the optimal spring stiffness to reduce the friction drag is in the range of $1 < \omega_0 < 5$.

Figure 9 (b) shows the time trace of the friction drag coefficient $C_{\tau x}$ for rigid and three compliant cylinders where the damping parameter ζ is changed. Among Cases 2-a to 2-j, the most effective case in reducing the friction drag is Case 2-a; *i.e.*, $\zeta = 0$, and the mean friction drag reduction rate is about 2.6%. Note that, although the friction drag reduction rate is maximum, the total drag is much increased in Case 2-a than other cases, since the pressure drag increase more than the reduction of the friction drag. Unfortunately, the total drag is increased to some degree in all cases we have tested. However, it is shown that the friction drag reduction is possible with a compliant surface, and it is expected that the total drag reduction is possible when the friction drag of the flow is dominant in total drag, as is often observed around a huge tanker and an airplane.

CONCLUSION

We have developed a direct numerical simulation code of the flow across a deformable bluff body. This code is constructed so that it can solve flow across a three-dimensional deformable obstacle. In order to investigate the influence of compliant surface on pressure and friction drag, flow across a compliant cylinder is calculated. As a first stage of the present study, a relatively low-Reynolds-number flow across a compliant cylinder is analyzed in order to verify the present code. The Strouhal number and wall pressure distribution are found to agree satisfactorily with experimental and numerical results in the literature.

Compliant surface is modelled in a mass, spring and damper system, and we have tested several cases changing the damping parameter and the spring stiffness. It is found

that the pressure drag is increased with compliant surface. When the non-dimensionalized spring stiffness is extremely small, pressure drag is increased drastically. On the other hand, although the total drag reduction is not observed in our cases, friction drag reduction is possible when the material properties is determined suitably. This fact indicates that a compliant surface can be applied as a drag reduction device in friction drag dominant flows, which is often observed around a huge ship.

REFERENCES

Bushnell, D. M., Hefner, J. N., and Ash, R. L., 1977, "Effect of Compliant Wall Motion on Turbulent Boundary Layers," *Phys. Fluids*, Vol. 20, pp. S31-S48.

Bushnell, D. M., and Hefner, J. N. (Eds.), 1990, Progress on Astronautics and Aeronautics, Viscous Drag Reduction in Boundary Layers, AIAA, New York, Vol. 123.

Carpenter, P. W., and Garrad, A. D., 1985, "The hydrodynamic stability of flow over Kramer-type compliant surfaces. Part 1. Tollmien-Schlichting instability," *J. Fluid Mech.*, Vol. 155, pp. 465-510.

Carpenter, P. W., and Morris, P. J., 1990, "The Effect of Anisotropic Wall Compliance on Boundary-Layer Stability and Transition," *J. Fluid Mech.*, Vol. 218, pp. 171-223.

Chu, H. H., and Blick, E. F., 1969, "Compliant Surface Drag as a Function of Speed," *J. Spacecraft and Rockets,* Vol. 6, pp. 763-764.

Demuren, A. O., and Ibraheem, S. O., 1998, "Multigrid method for the Euler and Navier-Stokes equations," *AIAA J.*, Vol. 36, pp. 31-37.

Endo, T., and Himeno, R., 2001, "Direct Numerical Simulation of Turbulent Flow Over a Compliant Surface," *Proc. 2nd Int. Symp. Turbulence & Shear Flow Phenomena*, Stockholm, Vol. 1, pp. 395-400.

Endo, T., and Himeno R., 2002, "Direct Numerical Simulation of Turbulent Flow Over a Compliant Surface," *Journal of Turbulence*, Vol. 3, 007. (http://www.stacks.iop.org/1468-5248/3/007).

Gad-el-Hak, M., 1996, "Modern Developments in Flow Control," *Appl. Mech. Rev.*, Vol. 49-7, pp. 365-379.

Gray, J., 1936, "Studies in Animal Locomotion. VI The Propulsive Powers of the Dolphin," *J. Exp. Biology*, Vol. 50, pp. 233-255.

Kasagi, N., 1998, "Progress in Direct Numerical Simulation of Turbulent Transport and Its Control," *Int. J. Heat & Fluid Flow*, Vol. 19, pp. 128-134.

Kawamura, K., and Kuwahara, K., 1984, Computation of high Reynolds number flow around a circular cylinder with surface roughness, *AIAA paper*: 84-0340.

Kovasznay, L. S. G., 1949, "Hot-Wire Investigation on the Wake Behind Cylinders at Low Reynolds Numbers," *Proc. Royal Soc. of London, A*, Vol. 198, 174-190.

Kramer, M. O., 1960, "Boundary Layer Stabilization by Distributed Damping," *Nav. Eng. J.*, Vol. 72, pp. 25-33.

Liu, H., Sunada, S., and Kawachi, K., 1995, "Time-Accurate Solutions to the Incompressible Navier-Stokes Equations with the Pseudo-Compressibility Method," in Numerical Developments in CFD, ASME, FED-Vol. 215, pp. 105-112.

Moin, P., and Bewley, T., 1994, "Feedback control of turbulence," *Appl. Mech. Rev.*, Vol. 47, pp. S3-S13.

Riley, J. J., Gad-el-Hak, M., and Metcalfe, R. W., 1988, "Compliant Coatings," *Annu. Rev. Fluid Mech.*, Vol. 20, pp. 393-420.

Thoman, D. C., and Szewczyk, A. A., 1969, "Time-Dependent viscous flow over a circular cylinder," *Phys. Fluids*, Vol. 12-II, pp. 76-87.

Tritton, D. J., 1959, "Experiments on the Flow Past a Circular Cylinder at Low Reynolds Numbers," *J. Fluid Mech.*, Vol. 6, pp. 547-567.